PCCP

PAPER

View Article Online
View Journal



Cite this: DOI: 10.1039/c5cp01175b

# Modulating the interaction between gold and $TiO_2$ nanowires for enhanced solar driven photoelectrocatalytic hydrogen generation†

P. Sudhagar,‡*[a] Taeseup Song,‡[b] Anitha Devadoss,[a] Jung Woo Lee,[c] Marta Haro,[d] Chiaki Terashima,[a] Volodymyr V. Lysak,[e] Juan Bisquert,[df] Akira Fujishima,[a] Sixto Gimenez*[d] and Ungyu Paik*[c]

The interaction strength of Au nanoparticles with pristine and nitrogen doped $TiO_2$ nanowire surfaces was analysed using density functional theory and their significance in enhancing the solar driven photoelectrocatalytic properties was elucidated. In this article, we prepared 4-dimethylaminopyridine capped Au nanoparticle decorated $TiO_2$ nanowire systems. The density functional theory calculations show {101} facets of $TiO_2$ as the preferred phase for dimethylaminopyridine–Au nanoparticles anchoring with a binding energy of $-8.282$ kcal mol$^{-1}$. Besides, the interaction strength of Au nanoparticles was enhanced nearly four-fold ($-35.559$ kcal mol$^{-1}$) at {101} facets *via* nitrogen doping, which indeed amplified the Au nanoparticle density on nitrided $TiO_2$. The Au coated nitrogen doped $TiO_2$ (N–$TiO_2$–Au) hybrid electrodes show higher absorbance owing to the light scattering effect of Au nanoparticles. In addition, N–$TiO_2$–Au hybrid electrodes block the charge leakage from the electrode to the electrolyte and thus reduce the charge recombination at the electrode/electrolyte interface. Despite the beneficial band narrowing effect of nitrogen in $TiO_2$ on the electrochemical and visible light activity in N–$TiO_2$–Au hybrid electrodes, it results in low photocurrent generation at higher Au NP loading ($3.4 \times 10^{-7}$ M) due to light blocking the N–$TiO_2$ surface. Strikingly, even with a ten-fold lower Au NP loading ($0.34 \times 10^{-7}$ M), the synergistic effects of nitrogen doping and Au NPs on the N–$TiO_2$–Au hybrid system yield high photocurrent compared to $TiO_2$ and $TiO_2$–Au electrodes. As a result, the N–$TiO_2$–Au electrode produces nearly 270 μmol h$^{-1}$ cm$^{-2}$ hydrogen, which is nearly two-fold higher than the pristine $TiO_2$ counterpart. The implications of these findings for the design of efficient hybrid photoelectrocatalytic electrodes are discussed.

Received 27th February 2015,
Accepted 12th June 2015

DOI: 10.1039/c5cp01175b

www.rsc.org/pccp

## Introduction

Semiconductor photocatalysis and photoelectrochemistry, particularly involving $TiO_2$, is an influential field that plays an important role on environmental remediation and energy conversion applications. The striking features of $TiO_2$ including its high chemical stability in aqueous media, high photoactivity, earth abundance and environmentally benign nature strongly encourage the use of this material as a potential electron acceptor in light driven devices operating under solar radiation.[1,2] The primary report on photoelectrocatalytic (PEC) water oxidation on $TiO_2$ by Fujishima and Honda[3] has promoted a huge body literature on the design of nanostructured photocatalytic materials for realizing the solar driven PEC water oxidation process.[4,5] Moreover, the photogenerated holes at the valence band of $TiO_2$ energetically favour the oxidation process of chemical components (like pollutants, *etc.*). This process can be understood as a renaissance of natural photosynthesis utilizing man-made materials. Nonetheless, the short wavelength cut-off property of $TiO_2$ permits accessing only a narrow segment ($\sim$5%) of the solar spectrum; resulting in low PEC efficiency.[6] Conversely, the VB edge position ($\sim$3.2 V *vs.* NHE) of $TiO_2$ meets the energy requirement for successful PEC water oxidation,

[a] *Photocatalysis International Research Center, Research Institute for Science & Technology, Tokyo University of Science, 2641 Yamazaki, Noda, Chiba 278-8510, Japan. E-mail: vedichi@gmail.com*
[b] *School of Materials Science and Engineering, Yeungnam University, Gyeongsan 712-749, Korea*
[c] *Department of Energy Engineering and Advanced Materials Science Engineering, Hanyang University, Seoul 133 791, South Korea. E-mail: upaik@hanyang.ac.kr*
[d] *Institute of Advanced Materials (INAM), Universitat Jaume I, 12071 Castelló, Spain. E-mail: sjulia@uji.es*
[e] *Department of Nanotechnology and Material Science, National Research University of Information Technologies, Mechanics and Optics, Saint Petersburg, Russia*
[f] *Department of Chemistry, Faculty of Science, King Abdulaziz University, Jeddah, Saudi Arabia*

† Electronic supplementary information (ESI) available: XRD, UPS and impedance results. See DOI: 10.1039/c5cp01175b

‡ These authors equally contributed to this research.

where most of the visible light band gap materials such as CdS, CdSe, GaAs, and GaP fall short.[7,8] Therefore, developing strategies to amplify the light harvesting efficiency of $TiO_2$ (greater than 5%) without sacrificing its PEC water oxidation potential is strongly in demand to further improve the PEC performance of $TiO_2$.

In this context, gold nanoparticle (Au NP) supported $TiO_2$ hybrid photocatalytic systems have attracted much attention because of their strong light absorption in the visible region, which arises from enhanced scattering and localized surface plasmon resonance (LSPR).[9–11] Due to LSPR, Au NPs can effectively harvest the electromagnetic energy of the incident light and concentrate it into ''plasmonic hotspots'', which in turn can maximize the local field intensity by a factor of $10^6$.[12] Notably, one dimensional (1-D) $TiO_2$ nanostructures such as nanowires, nanotubes, nanofibers, *etc.* afford ample room to accommodate the nanoparticles compared to their bulk counterparts.[13] Moreover, the rapid electron transport in the 1-D $TiO_2$ crystallite framework is highly beneficial for the efficient charge collection at the relevant interfaces.[14,15] In the case of $TiO_2$–Au hybrid photocatalytic systems, neither individual Au NPs nor $TiO_2$ can act as an efficient photocatalyst upon visible-light irradiation,[16] but a proper combination of both materials generates excellent visible-light PEC performances, even significantly enhancing the UV photocatalysis of $TiO_2$.[17–21] This indicates that the interfacial interaction between Au NPs and $TiO_2$ plays a key role in achieving optimum PEC performance.

So far, a number of strategies have been documented in the literature for anchoring the Au NPs on $TiO_2$ surfaces. For instance, Au NPs were coated on $TiO_2$ *via* physical evaporation or sputtering resulting in the formation of inhomogenous NP coating on the metal oxide host surface.[22,23] Alternatively, it has been reported that Au NPs can also be deposited on $TiO_2$ substrates *via* directly reducing gold salts by chemical reduction or photodeposition.[24–28] Unfortunately, such deposition techniques affect the supporting semiconductors due to the multiple post-treatment steps. Similarly, controlling the size, shape and distribution of Au NPs using such approaches still remains challenging. Recently, we have demonstrated a straightforward method of anchoring 4-dimethylaminopyridine (DMAP) capped Au NPs on $TiO_2$ hollow nanowires, which in turn resulted in enhanced photocatalytic performance towards dye degradation.[29] In the present study, we investigate the underlying mechanism behind the single-step anchoring of DMAP capped Au NPs on $TiO_2$ nanowires and their respective interactions were studied using theoretical simulations based on first principle theory. The interaction between DMAP capped Au NPs and $TiO_2$ nanowires was modulated *via* nitrogen doping $TiO_2$. The influence of nitrogen doping and DMAP capped Au NPs anchoring on $TiO_2$ band modification was elucidated. The finite-difference time domain (FDTD) method was used to quantitatively analyse the electromagnetic field enhancement in the $TiO_2$–Au hybrid photocatalytic system. Our theoretical and experimental results demonstrate the synergistic effect of Au NPs (visible light scattering) and nitrogen doping (band gap narrowing effect) on the PEC water oxidation process and the implications of these findings are discussed.

# Experimental

## Materials

All materials were received from Sigma-Aldrich and used as received.

## Fabrication of $TiO_2$ nanowire arrays

Vertically aligned $TiO_2$ hollow nanowires onto FTO substrates were grown using ZnO nanorod array templates. First step, ZnO film of 200 nm was deposited on the FTO substrate using radio frequency magnetron sputtering. Following that, the ZnO seed layer coated FTO substrate was immersed into aqueous solution of 0.025 M zinc nitrate hexahydrate and 0.025 M hexamethylenetetramine and the sample was kept at 85 °C for 10 h for the growth of vertically aligned ZnO nanorod arrays. After ZnO nanorod growth, the substrates were rinsed with deionized water.

In the second step, the $TiO_2$ layer will be grown on ZnO nanorod arrays as follows: the resultant ZnO NR array template was kept in aqueous solution of 0.075 M ammonium hexafluorotitanate and 0.2 M boric acid. This chemical bath deposition results in the thin layer of $TiO_2$ coating ZnO nanorods. Subsequently, the $TiO_2$ coated ZnO electrode is immersed in a 0.5 M boric acid solution for 1 h and the ZnO template is removed and rinsed with deionized water. Finally, vertically aligned $TiO_2$ NW arrays are obtained. The $TiO_2$ NW samples were calcined at 500 °C for 0.5 h under an Ar atmosphere.

For nitridation onto $TiO_2$ NWs, the electrodes were transferred to a chemical vapour deposition (CVD) chamber. The nitridation process was carried out at 500 °C with $H_2$ and $NH_3$ with flow rates of 50–200 standard cubic centimetre per minute (sccm) and 100–300 sccm, respectively.

## Synthesis of Au NPs

DMAP-capped Au NPs were synthesized using the phase transfer procedure.[30] Briefly, 0.030 M aqueous solution of $HAuCl_4{\cdot}3H_2O$ was added to 0.025 M tetraoctylammonium bromide (TOAB) in toluene. Then, 0.4 M aqueous $NaBH_4$ was added drop-wise to the mixture with stirring, causing an immediate reduction to occur. After 24 h, the two phases were separated and the toluene phase was subsequently washed with 0.1 M $H_2SO_4$, 0.1 M NaOH, and $H_2O$ (three times), and then dried over anhydrous $Na_2SO_4$. An equal volume of 0.1 M aqueous solution of DMAP was then added. The phase transfer is clearly visible as the dark pink coloured solution transfers from toluene to water due to the addition of DMAP and was completed within 1 h. Assuming a 100% efficient reduction of gold chloride and no losses during transfer and washing steps, the particle size yields a particle concentration of approximately $6.8 \times 10^{-7}$ M in the stock solution arising from the nanoparticle synthesis.

## Assembly of Au NPs on $TiO_2$ nanowire arrays

Au NP coating on $TiO_2$ and N–$TiO_2$ NW arrays was obtained by immersing the $TiO_2$ electrodes in positively charged, water soluble DMAP-capped Au NP solution ($3.4 \times 10^{-7}$ M) for 5 min. The positively charged DMAP-capped Au NPs were attracted towards the negatively charged surface of $TiO_2$ NWs and N–$TiO_2$ NWs,

 

resulting in the facile formation of electrostatically assembled $TiO_2$–Au and N–$TiO_2$–Au hybrid photocatalytic electrodes. After coating Au NPs on these electrodes DMAP molecules were removed by the sintering process.

### Theoretical calculations

The energy calculations were performed using the PW91 method generalized gradient approximation (GGA) and the plane wave model using CASTEP program. The supercell of 20 Å $\times$20 Å $\times$ $c$ was used for the calculation, which represents the nanowire length along the tube axis as $c$. All atoms were described using Vanderbilt ultrasoft pseudopotentials and a cut off energy of 240 eV where a set of $k$-points was used to expand the electronic wave function based on the Monkhorst–Pack scheme within $5.0 \times 10^{-5}$ eV per atom of total energy convergence. Electron density was investigated with optimized geometries. The binding energies of atoms on the nanotubes were calculated by eqn (1)

$$E_b = E_{nanotube+atom} - (E_{nanotube} + E_{atom}). \quad (1)$$

### Structural and optical characterization

The surface of various $TiO_2$ nanowire arrays was characterized using a field emission scanning electron microscope (FE-SEM, JEM-3100F, Jeol, Tokyo, Japan) and a field emission transmission electron microscope (FE-TEM, JSM 7600F, JEOL, Tokyo, Japan). The chemical environment of pure and N doped $TiO_2$ electrodes was analyzed by X-ray photoelectron spectroscopy (XPS) using an angular resolved electron analyzer with a monochromated Al Kα source (Theta Probe, Thermo Fisher Scientific). The optical diffuse reflectance spectra of the electrodes were recorded in the range of 350–900 nm using a V670 JASCO UV-Vis spectrophotometer. The absorbance of the electrodes was estimated from diffuse reflectance measurements ($R$) directly using the Kubelka–Munk relation, $F.R. = (1 - R)^2/2R$ using in built software from a JASCO UV-Vis spectrometer. We have assumed that the scattering term is similar for photoelectrodes with and without Au loading.

### (Photo)-electrochemical characterization

The (photo)-electrochemical analysis was done using a three electrode configuration. The as-prepared $TiO_2$, $TiO_2$–Au, N–$TiO_2$ and N–$TiO_2$–Au electrodes (electrode area 1 $cm^2$) were used as the working electrode, Ag/AgCl as the reference and Pt foil as the counter electrode. 0.5 M of $Na_2SO_4$ (Sigma Aldrich) (pH = 6.1) was used as the electrolyte for all PEC measurements without any additional additives. Cyclic voltammograms were recorded using an advanced potentiostat (PGSTAT-30 from Autolab) with a scanning rate of 50 mV $s^{-1}$. The photocurrent measurements were recorded using a solar simulator with a 300 W xenon arc-lamp (Hayashi- LA 251-Xe). The light intensity was calibrated using a silicon photodiode (100 mW $cm^{-2}$). The electrolyte was bubbled with nitrogen gas for 30 min to avoid the presence of oxygen (electron acceptor) in the solution. The IPCE measurements were carried out by employing a 300 W Xe lamp coupled to a computer-controlled monochromator; the photoelectrode was polarized at the desired voltage (1.6 V *vs.* RHE) using a Gamry potentiostat, and the photocurrent was measured using an optical power meter 70 310 from Oriel Instruments. A Si photodiode was used to measure the light intensity to calibrate the system. The output gas samples were collected from the head space of a sealed PEC chamber using an air-tight gas syringe through the manual sampling port in the top of the chamber (flexible cork made of Teflon) and further subjected to gas chromatographic analysis to evaluate the constituents of the gas products.

## Theoretical calculations

To get insights into the binding mechanism of positively charged DMAP-capped Au NPs on $TiO_2$ NWs and N–$TiO_2$ NWs, it is important to estimate the binding energies in the hybrid systems. First principles based simulations provide direct evidence of interaction energies between DMAP–Au NPs and the $TiO_2$ semiconductor, which can be used to detect the optimal binding sites and to predict the maximal affinity that a nanoparticle could attain from them. The binding characteristics in $TiO_2$–Au and N–$TiO_2$–Au hybrid photocatalytic systems were analyzed using first principles theory. Firstly, the binding energies between molecular DMAP and Au were estimated. It was found that the DMAP molecule strongly binds to gold with $-14.01$ kcal $mol^{-1}$ binding energy, which could be ascribed to the high binding affinity of Au atoms towards the pyridine moieties in DMAP.

Recent studies show that the photocatalytic activity of $TiO_2$ strongly depends on its crystal facets.[31–33] Moreover, it was realized that the deposition of metal nanoparticles (Ag, Au and Pt) onto selective {101} facets of anatase $TiO_2$ crystals with different percentages of exposed {001} and {101} facets can effectively enhance the photocatalytic activity of $TiO_2$ in both photoreduction and photo-oxidation processes.[34,35] In this line, we examined the binding nature of DMAP–Au NPs on {101} and {001} facets of $TiO_2$. Fig. 1 shows the optimal binding sites of DMAP–Au NPs on (a) {001} facets and (b) {101} facets of $TiO_2$. The {101} facet of $TiO_2$ shows higher binding energy ($-8.282$ kcal $mol^{-1}$) towards DMAP–Au NP anchoring compared to the {001} facets of $TiO_2$ ($-6.48$ kcal $mol^{-1}$), illustrating the higher affinity of {101} surfaces towards DMAP–Au NP anchoring. Fig. 1c shows the density of the electron cloud at the $TiO_2$–Au hybrid electrode.

The reported excellent catalytic activity and band structure modifications of $TiO_2$ upon nitrogen doping[36–39] inspired us to investigate the effect of nitrogen doping on DMAP–Au NP binding. Fig. 1(d–f) show the binding orientations and density of electron cloud distribution in N–$TiO_2$–Au hybrid electrodes. As anticipated, higher binding energies ($-8.86$ kcal $mol^{-1}$) were observed for DMAP–Au NPs anchoring on N–$TiO_2$ than on pristine $TiO_2$ NWs ($-6.48$ kcal $mol^{-1}$) at the {001} surface. This could be ascribed to the higher binding affinity of pyridines and Au towards nitrogen. Strikingly, the binding energies were found to be remarkably enhanced at the {101} surface of N–$TiO_2$ NWs. The N–$TiO_2$–Au hybrid system shows a binding energy of $-35.56$ kcal $mol^{-1}$ at the {101} surface, which is nearly

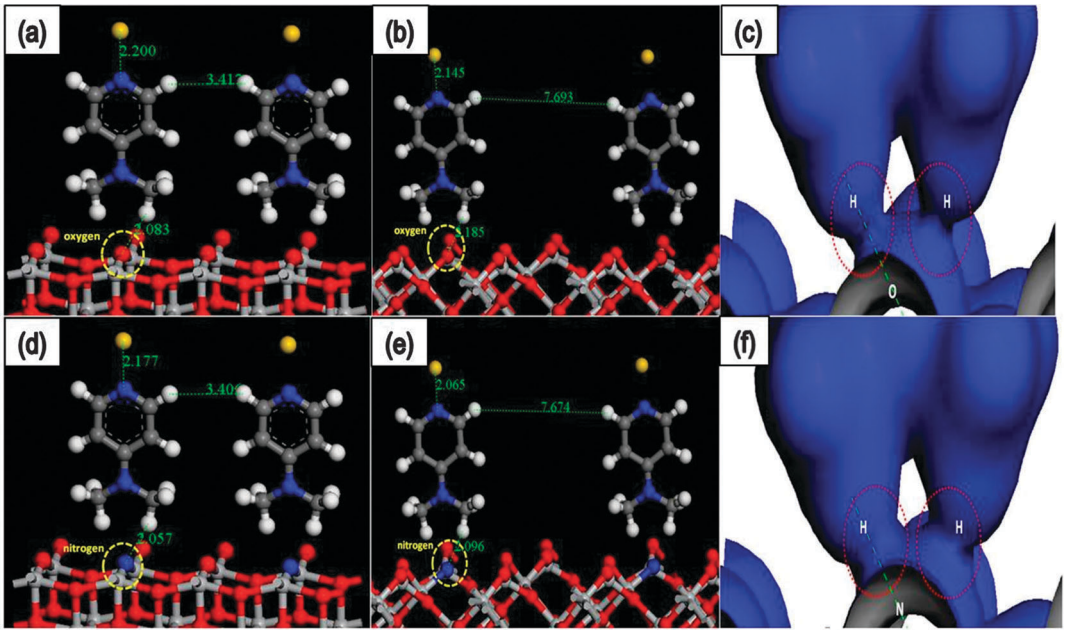


Fig. 1 The optimal orientations of $TiO_2$ (a and b) and N–$TiO_2$ (d and e) surfaces illustrating the binding mechanism of DMAP–Au NPs at {001} and {101} planes, respectively. The electron density distribution estimated at $TiO_2$–Au (c) and N–$TiO_2$–Au (f) electrodes.

four times higher than that observed for the {001} plane of N–$TiO_2$ NWs. This strongly suggests that the Au NPs can be effectively coated onto N–$TiO_2$ by electrostatic attraction.

On the other hand, in view of improving the light harvesting efficiency of $TiO_2$, Au NP decoration found to improve the visible light activity of hybrid materials owing to their strong scattering effect and enhanced absorption at around 520 nm due to the LSPR band. To understand the origin and the extent of improved visible light activity in $TiO_2$–Au hybrid systems, the light scattering effect of Au NPs at $TiO_2$ NWs was further analyzed using the finite-difference time-domain (FDTD). Fig. 2 shows the electric field (E-field) distribution in the perpendicular direction, across the Au NPs at the $TiO_2$-NW surface obtained from FDTD simulations. The permittivity of gold was analyzed using the Lorenz–Drude dispersive model.[40]

$$\varepsilon_r(\omega) = \varepsilon_{r,\infty} + \sum_{m=0}^{5} \frac{G_m \Omega_m{}^2}{\omega_m{}^2 - \omega^2 + j\omega\Gamma_m} \quad (2)$$

where $\varepsilon_r(\omega)$ is the relative permittivity at infinity frequency, $G_m$ is the strength of each resonance term, $\Omega_m$ is the plasma frequency, $\omega$ and $\omega_m$ are the angular and resonant frequency, respectively, and $\Gamma_m$ is the damping factor or collision frequency. Fig. 2(a) and (b), clearly illustrate the electric field generation around the Au NPs. The electric field extension varies with Au NP loading (spacing) on $TiO_2$. The visible light scattering centres around Au NPs transformed the light reception at $TiO_2$. However, higher loadings of Au NPs on $TiO_2$ found to scatter the major portion of input light, which may reduce the light transmission reaching the $TiO_2$ surface. Thus, it is anticipated that the $TiO_2$–Au hybrid system benefits not only from improved LSPR band facilitated absorption at 520 nm,

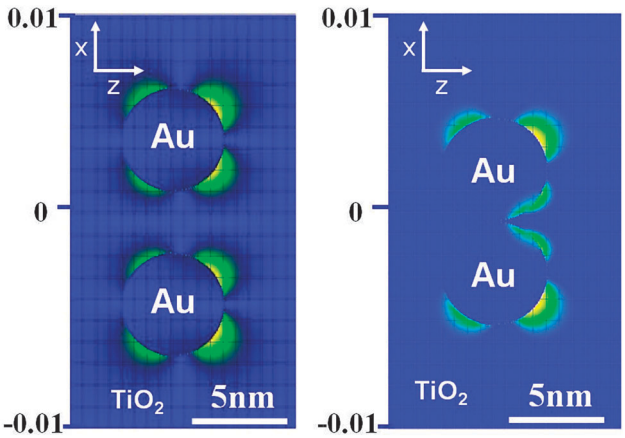


Fig. 2 Spatial distribution of electric-field energy density of the $TiO_2$–Au hybrid photocatalytic system under different spacing conditions: (a) with a few nm spacings and (b) Au nanoparticles in contact (the *y* axis indicates the distance in nm).

but also from the light scattering effect of Au NPs, which could effectively improve the light absorption properties of $TiO_2$ itself.

## Experimental results

From the above discussion, it is inferred that the Au NP decoration at $TiO_2$ NWs could yield high PEC energy conversion efficiency, mainly through light scattering and co-catalyst effects. Moreover, nitrogen doping was found to enhance the interaction between Au NPs and $TiO_2$ as well as the visible light activity of $TiO_2$ by the band gap narrowing effect.[39] In order to understand the role of Au NP decoration and nitrogen doping,

we have designed and fabricated Au NP decorated $TiO_2$ NW and N–$TiO_2$ NW arrays onto fluorinated tin oxide (FTO) substrates. Fig. 3 shows the electron microscopy images of nitrided $TiO_2$ (N–$TiO_2$) NW, Au NP coated $TiO_2$ NW ($TiO_2$–Au) and N–$TiO_2$ NW (N–$TiO_2$–Au) arrays, respectively.

Scanning electron microscopy (SEM) and transmission electron microscopy (TEM) images of N–$TiO_2$ NWs clearly reveal their vertically aligned geometry and 1-D structure (Fig. 3a). The N–$TiO_2$ NWs have a length of ~5 μm, an inner free space of ~200 nm and a shell thickness of ~50 nm, respectively (Fig. 3b). From Fig. 3c and d, a thin amorphous layer is observed on $TiO_2$. This layer represents the formation of TiN/$TiO_xN_y$ on the $TiO_2$ NW surface during the nitridation process. Although it was difficult to obtain lattice resolved TEM images at the surface of N–$TiO_2$ NWs, the X-ray diffraction (XRD) and SAED patterns support that N–$TiO_2$ NWs maintain their polycrystalline anatase phase (see ESI,† Fig. S1). There are no noticeable changes in the geometry of the NWs after Au NP anchoring (Fig. 3f and j). Au NPs with an average diameter of ~5 nm were observed in the high magnification TEM images (Fig. 3i) (also see ESI,† Fig. S2). These images (Fig. 3h and l) confirm the higher loading of Au NPs on N–$TiO_2$ NWs compared to pristine $TiO_2$ NWs.

The effect of nitrogen doping on $TiO_2$ NWs was studied by X ray photoelectron spectroscopy. Fig. 4(a) shows the core spectra of Ti 2p in pristine $TiO_2$ NWs and N–$TiO_2$ NWs. The shoulder peaks at 459.4 eV and 465.1 eV correspond to Ti $2p_{3/2}$ and Ti $2p_{1/2}$, respectively.[41] In N–$TiO_2$ NWs, these peaks were shifted toward lower binding energy indicating the successful nitrogen doping at the $TiO_2$ NWs. Upon further examining the N 1s core spectra (Fig. 4b), the peaks at 396.8, 398.8, and 400.6 eV provide a clear picture of the nitrogen environment at $TiO_2$ NWs. The peak at 396.8 eV is attributed to the existence of atomic β-N in the $TiO_2$ matrix and the peak at 398.8 eV implies the substitution of $O_2^-$ by nitrogen ions and thus, results in the formation of N–Ti–O.[42,43] This confirms the existence of $Ti^{3+}$ due to the incorporation of nitrogen atoms into oxygen lattice sites. The weaker peak at 400.6 eV indicates the interstitial doping which induces an additional impurity state above the valence band of $TiO_2$.[44] The atomic ratio of nitrogen doping carriers was estimated from Fig. 4b and found to be 5.8 wt%. The broad features of the O 1s peak in Fig. 4c were deconvoluted using the Gaussian fit (Fig. 4c, inset). Three distinct peaks were observed at 530.9, 532.2 and 533.2 eV representing the lattice oxygen, surface hydroxyl oxygen and surface adsorbed oxygen, respectively. The atomic weight of lattice oxygen at $TiO_2$ NWs was estimated to be 51.5%, which was reduced to 47.6% upon nitrogen doping. This indicates the possibility of nitrogen atoms occupying the oxygen vacancies. The influence of nitrogen doping on the work function of $TiO_2$ NWs was examined using ultraviolet photoelectron spectroscopy (see ESI,† Fig. S3). The valence band maximum (VBM) position of $TiO_2$ NWs at ~3.26 eV was shifted to ~2.69 eV upon nitrogen doping. This indicates that nitrogen doping carriers

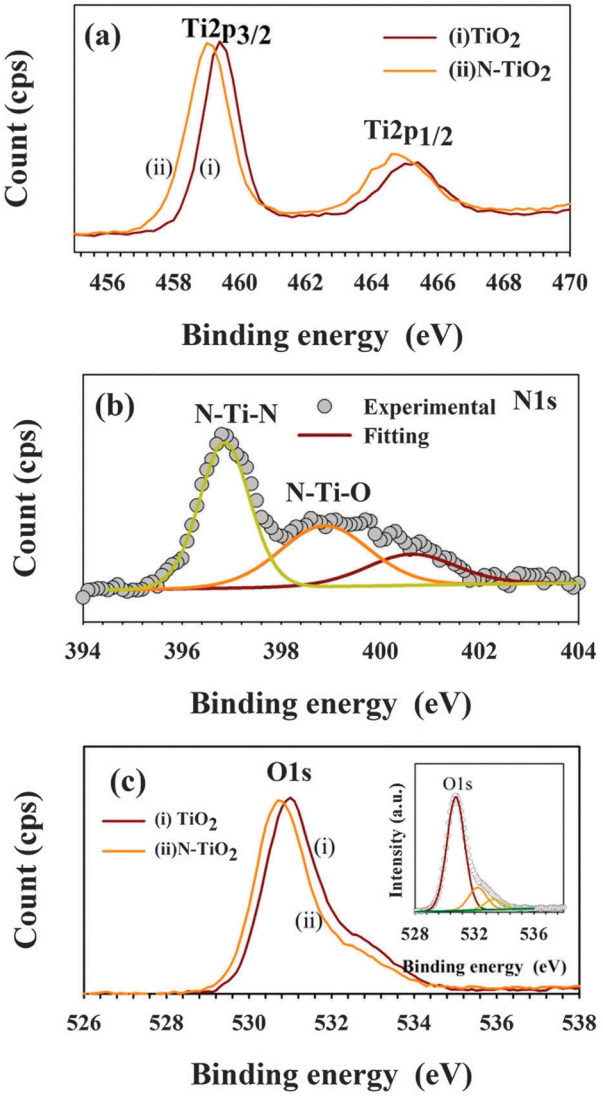


Fig. 4 XPS results of (a) Ti 2p, (b) N 1s and (c) O 1s core spectra of $TiO_2$ and N–$TiO_2$ electrodes.

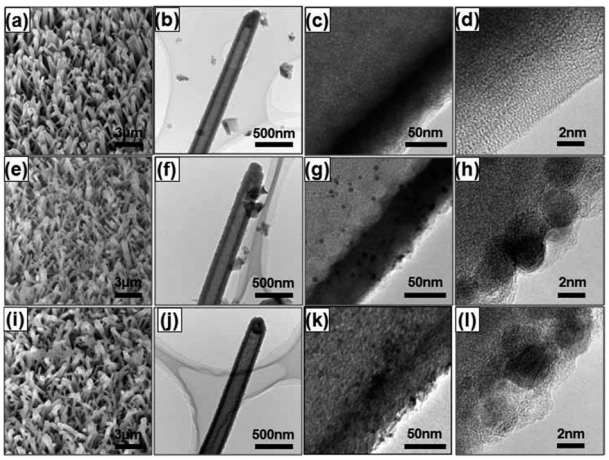


Fig. 3 SEM images of (a) N–$TiO_2$, (e) $TiO_2$–Au and (i) N–$TiO_2$–Au electrodes. The TEM images (b–d), (f–h), and (j–l) represents the high magnification TEM images corresponding to N–$TiO_2$, $TiO_2$–Au and N–$TiO_2$–Au electrodes, respectively.

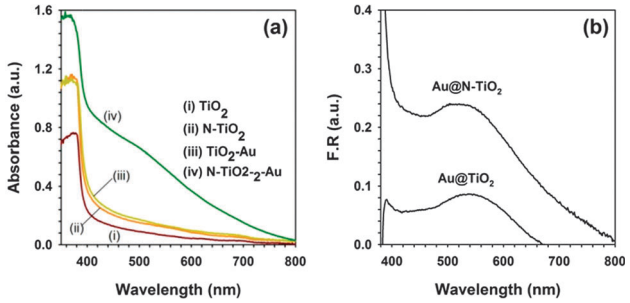


Fig. 5 (a) Absorbance spectra of $TiO_2$ and N–$TiO_2$ electrodes in the presence and the absence of Au NPs; (b) Kubelka–Munk relation of Au NPs decorated at $TiO_2$ NWs and N–$TiO_2$ NWs.

are creating sub-bands or defects above the VB of $TiO_2$ as discussed in the XPS results.

In order to study the contribution of DMAP–Au NPs towards the visible light activity of $TiO_2$–Au and N–$TiO_2$–Au hybrid photocatalysts, diffuse reflectance measurements were performed. The results are shown in Fig. 5a. The Kubelka–Munk absorbance contribution of $TiO_2$ NWs and N–$TiO_2$ NWs was subtracted from the absorbance spectrum of $TiO_2$–Au and N–$TiO_2$–Au hybrids, respectively (Fig. 5b). Both spectra confirm the enhanced scattering induced by the presence of Au NPs, being the LSPR effect negligible for these specimens. Although, Au NP coating at $TiO_2$ and N–$TiO_2$ was carried out under identical conditions, N–$TiO_2$–Au hybrid electrodes showed higher absorbance, indicating higher loading of Au NPs in good correspondence with the TEM measurements (Fig. 2h and l) and the Kubelka–Munk function (*F.R.*) (inset of Fig. 5). This is attributed to the higher binding energy observed at the N–$TiO_2$ surfaces. The broad absorption nature of N–$TiO_2$–Au may be originated from the light scattering effect which amplifies the absorbance of $TiO_2$.[45]

To test the photoelectrochemical (PEC) water oxidation performance, we measured *J–V* characteristics of these electrodes under the dark and illumination conditions. From Fig. 6a, it was found that the $TiO_2$–Au hybrid electrode showed four times higher photocurrent $\sim$0.4 mA $cm^{-2}$ than the pristine $TiO_2$ NW electrode (0.11 mA $cm^{-2}$). This photocurrent enhancement may be due to the combined effect of higher optical absorption due to the scattering and co-catalytic effect of Au NPs in water oxidation through the formation of the Au–$TiO_2$ Schottky junction.[46,47] In addition, it may facilitate the charge separation at $TiO_2$/electrolyte interfaces and thus reduces the recombination of electrons through surface states of $TiO_2$.[48] In the case of nitrogen doping at $TiO_2$ NWs, the photocurrent density was slightly enhanced (0.22 mA $cm^{-2}$), which might be ascribed to the promotion of visible light activity of $TiO_2$ through the band gap narrowing effect (see ESI,† S3 and S4).

In striking contrast, the photocurrent in the N–$TiO_2$–Au hybrid system was only slightly higher than that in the N–$TiO_2$ NW system. This might be due to excessive Au NP decoration (from Fig. 3l), which may result in forward light scattering blocking the light photons reaching the N–$TiO_2$ NW surface and also reduce the interfacial contact between N–$TiO_2$ and FTO electrodes, thus hindering the photoholes participating in the

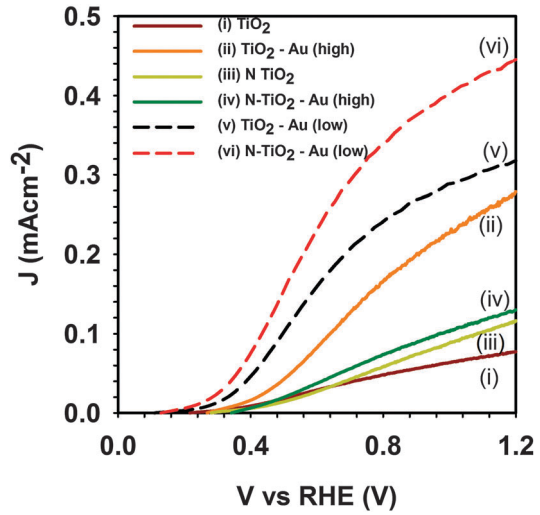


Fig. 6 *J–V* results of PEC water splitting using different photoanode electrodes. Note that two different Au concentrations were used for decorating working electrodes: (low – 0.34 $\times$ $10^{-7}$ M; high – 3.4 $\times$ $10^{-7}$ M).

water oxidation process.[18] This implies that there exists a trade-off between the enhanced light scattering due to Au NP decoration and visible light photon reception at N–$TiO_2$ NWs, which necessitates the optimization of Au NP loading onto N–$TiO_2$ NWs. We have recently reported that the photoelectrochemical performance of $TiO_2$–Au nanocomposites has a volcano dependence with Au loading.[28]

Interestingly, the Au NP decorated $TiO_2$ and N–$TiO_2$ electrodes using low concentration stock solution (0.34 $\times$ $10^{-7}$ M), here referred to as $TiO_2$–Au (low) and N–$TiO_2$–Au (low), respectively, lead to higher photocurrent compared to the high Au concentration samples, as observed in Fig. 6. This photocurrent enhancement strongly suggests minimizing the optical blocking effect through controlling the Au NP loading on N–$TiO_2$.

Furthermore, the stability of electrodes in photocurrent generation is examined with chronoamperometric curves (see ESI,† S5). The significant decrease of the photocurrent in both $TiO_2$ and $TiO_2$–Au electrodes may be attributed to the current leakage at $TiO_2$/FTO interfaces to the electrolyte through the naked FTO surface (uncovered $TiO_2$ area). Another plausible reason may arise from Au stability under long time photo-irradiation. However it is not clear at this moment and further research on this topic is needed. It is anticipated that inserting a compact $TiO_2$ blocking layer between $TiO_2$ and FTO layers will hinder the electron flow from the charge collector to the electrolyte.

In order to further corroborate the absence of the plasmonic effect at Au coated $TiO_2$ electrodes, we recorded IPCE spectra (see ESI,† Fig. S6). There is no photocurrent peak at around 550 nm in the $TiO_2$–Au electrode as observed in optical absorption spectra (Fig. 5b). This implies that there is no electron injection from Au nanoparticles to $TiO_2$ by the plasmonic effect. Instead, Au NPs are promoting the optical absorption of $TiO_2$ through the scattering effect. In addition, Au NPs play a critical role as a co-catalyst in the water oxidation process as shown in Fig. S4 (ESI†). The photoholes generated at the

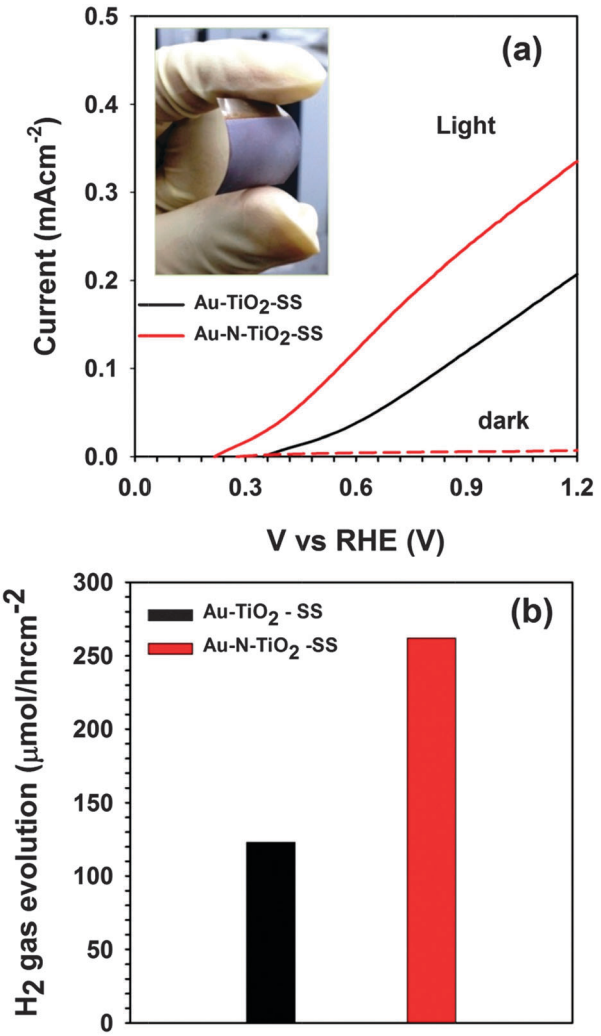


Fig. 7 (a) *J–V* characteristics of PEC water splitting with different photoanodes (inset: a photograph of N–$TiO_2$–Au on the flexible SS substrate) and (b) hydrogen gas evolution from PEC experiments using different photoanodes.

valence band of $TiO_2$ and N–$TiO_2$ are injected into Au NPs and may oxidize the water molecules into oxygen and protons.

Aiming at the technological exploitation of the photocurrent enhancement due to nitrogen doping and loading of Au nanoparticles, we carried out the deposition of these structures on flexible stainless steel (SS) substrates. The flexible photoelectrodes are highly promising in solar-to hydrogen fuel production owing to their lower weight and cost, compared to FTO, together with more versatile mechanical properties. However, the $TiO_2$ nanowire fabrication onto flexible SS substrates remains challenging. A similar deposition procedure of $TiO_2$ on FTO substrates explained in the Experimental section was repeated for fabricating $TiO_2$ NWs on flexible SS substrates. We adopt the optimized Au NP concentration condition ($0.34 \times 10^{-7}$ M) from Fig. 6, and reconstructed the $TiO_2$–Au hybrid systems onto flexible stainless steel (SS) substrates instead of FTO substrates (the sample photo is presented in the inset of Fig. 7a).

The *J–V* characteristics of Au–$TiO_2$–SS and N–$TiO_2$–Au–SS electrodes were tested in the 0.5 M $Na_2SO_4$ aqueous electrolyte with a three electrode PEC cell step up. The *J–V* characteristic of N–$TiO_2$–Au–SS is displayed in Fig. 7a. The higher photocurrent density achieved in N–$TiO_2$–Au–SS compared to the $TiO_2$–Au–SS electrode agrees well with the trends presented in Fig. 6. The scattering effect by Au NPs, the band gap narrowing effect by N doping and catalysis at optimal concentration lead to high photocurrent generation at the N–$TiO_2$–Au–SS sample. A small onset potential shift occurred in this sample towards the negative potential region, also in good agreement with the results shown in Fig. 6. We believe that this cathodic shift can be related to enhanced charge collection at the contact for the N–doped $TiO_2$.

The gas evolution from the PEC water oxidation experiment was collected for one hour under light illumination at 1 V *vs.* RHE potential, and analysed using gas chromatography (Fig. 7b). It is observed that $TiO_2$–Au–SS hybrid electrodes could generate hydrogen of about 120 µmol $h^{-1}$ $cm^{-2}$. Interestingly, the hydrogen generated at N–$TiO_2$–Au–SS hybrid electrodes was about 270 µmol $h^{-1}$ $cm^{-2}$. The described bendable architecture of N–$TiO_2$–Au on SS substrates (inset of Fig. 7a) with light weight and low cost can be beneficial for large scale flexible PEC fuel generation.[49,50] Another advantage of both side conducting nature of SS substrates enables us to design an artificial leaf based (back side coated with the electrocatalyst) on monolithic wireless type solar fuel cells.[51]

## Conclusions

Hybrid photocatalytic systems developed by anchoring DMAP–Au NPs on N–$TiO_2$ nanowires exhibit interesting optical and photocatalytic properties for water oxidation. Nitrogen doping of $TiO_2$ both maximizes the DMAP–Au NP loading and improves the optical absorption due to the band narrowing effect. DMAP–Au NP anchoring amplifies the visible light activity of $TiO_2$ and N–$TiO_2$ *via* a light scattering effect and also improves the charge recombination at the electrode/electrolyte interface. After optimization of the Au loading on the nanostructured photoelectrodes, N-doped $TiO_2$ leads to enhanced photocurrent generation and slightly more favourable onset potential on both FTO and SS substrates. Hydrogen generation measured on films deposited on flexible SS substrates was significantly higher on N-doped $TiO_2$ nanostructures.

## Acknowledgements

This work was supported by the Global Research Laboratory (GRL) Program (K20704000003TA050000310) through the National Research Foundation of Korea (NRF) funded by the Ministry of Science. One of the authors P.S. acknowledges the financial support from Japan Society for the Promotion of Science (JSPS) for providing a Postdoctoral Research Fellowship. We also acknowledge the financial support from University Jaume I through the project P1·1B2014-51 project. We thank Dr Ivan Mora Sero for his fruitful suggestions for shaping this work. This work is partly supported by the Government of the Russian Federation (Grant 074-U01) through ITMO Early Carrier Fellowship scheme.

## Notes and references


1 A. L. Linsebigler, G. Lu and J. T. Yates, *Chem. Rev.*, 1995, **95**, 735–758.
2 P. V. Kamat, *J. Phys. Chem. C*, 2012, **116**, 11849–11851.
3 A. Fujishima and K. Honda, *Nature*, 1972, **238**, 37–38.
4 M. A. Fox and M. T. Dulay, *Chem. Rev.*, 1993, **93**, 341–357.
5 A. Kudo and Y. Miseki, *Chem. Soc. Rev.*, 2009, **38**, 253–278.
6 S. U. M. Khan, M. Al-Shahry and W. B. Ingler, *Science*, 2002, **297**, 2243–2245.
7 M. Gratzel, *Nature*, 2001, **414**, 338–344.
8 L. Yang, H. Zhou, T. Fan and D. Zhang, *Phys. Chem. Chem. Phys.*, 2014, **16**, 6810–6826.
9 D. Pile, *Nat. Photonics*, 2013, **7**, 3.
10 S. Linic, P. Christopher and D. B. Ingram, *Nat. Mater.*, 2011, **10**, 911–921.
11 P. Christopher, H. Xin, A. Marimuthu and S. Linic, *Nat. Mater.*, 2012, **11**, 1044–1050.
12 C. Clavero, *Nat. Photonics*, 2014, **8**, 95–103.
13 P. Rodenas, T. Song, P. Sudhagar, G. Marzari, H. Han, L. Badia-Bou, S. Gimenez, F. Fabregat-Santiago, I. Mora-Sero, J. Bisquert, U. Paik and Y. S. Kang, *Adv. Energy Mater.*, 2013, **3**, 176–182.
14 P. Sudhagar, V. Gonzalez-Pedro, I. Mora-Sero, F. Fabregat-Santiago, J. Bisquert and Y. S. Kang, *J. Mater. Chem.*, 2012, **22**, 14228–14235.
15 H. Han, P. Sudhagar, T. Song, Y. Jeon, I. Mora-Sero, F. Fabregat-Santiago, J. Bisquert, Y. S. Kang and U. Paik, *Chem. Commun.*, 2013, **49**, 2810–2812.
16 J.-J. Chen, J. C. S. Wu, P. C. Wu and D. P. Tsai, *J. Phys. Chem. C*, 2010, **115**, 210–216.
17 Z. W. Seh, S. Liu, M. Low, S.-Y. Zhang, Z. Liu, A. Mlayah and M.-Y. Han, *Adv. Mater.*, 2012, **24**, 2310–2314.
18 Y.-C. Pu, G. Wang, K.-D. Chang, Y. Ling, Y.-K. Lin, B. C. Fitzmorris, C.-M. Liu, X. Lu, Y. Tong, J. Z. Zhang, Y.-J. Hsu and Y. Li, *Nano Lett.*, 2013, **13**, 3817–3823.
19 K. Kim, P. Thiyagarajan, H.-J. Ahn, S.-I. Kim and J.-H. Jang, *Nanoscale*, 2013, **5**, 6254–6260.
20 M. A. Nadeem, M. Murdoch, G. I. N. Waterhouse, J. B. Metson, M. A. Keane, J. Llorca and H. Idriss, *J. Photochem. Photobiol., A*, 2010, **216**, 250–255.
21 Z. Zhang, L. Zhang, M. N. Hedhili, H. Zhang and P. Wang, *Nano Lett.*, 2012, **13**, 14–20.
22 V. S. K. Chakravadhanula, C. Kübel, T. Hrkac, V. Zaporojtchenko, T. Strunskus, F. Faupel and L. Kienle, *Nanotechnology*, 2012, **23**, 495701.
23 F. Liu, C. Tang, Z. Wang, C. Sui and H. Ma, *Nanotechnology*, 2014, **25**, 125703.
24 J. A. Ortega Méndez, C. R. López, E. Pulido Melián, O. González Díaz, J. M. Doña Rodríguez, D. Fernández Hevia and M. Macías, *Appl. Catal., B*, 2014, **147**, 439–452.
25 Y.-F. Yang, P. Sangeetha and Y.-W. Chen, *Int. J. Hydrogen Energy*, 2009, **34**, 8912–8920.
26 A. Tanaka, S. Sakaguchi, K. Hashimoto and H. Kominami, *Catal. Sci. Technol.*, 2014, **4**, 1931–1938.
27 E. Pedrueza, J. L. Valdés, V. Chirvony, R. Abargues, J. Hernández-Saz, M. Herrera, S. I. Molina and J. P. Martínez-Pastor, *Adv. Funct. Mater.*, 2011, **21**, 3502–3507.
28 M. Haro, R. Abargues, I. Herraiz-Cardona, J. Martínez-Pastor and S. Giménez, *Electrochim. Acta*, 2014, **144**, 64–70.
29 P. Sudhagar, A. Devadoss, T. Song, P. Lakshmipathiraj, H. Han, V. V. Lysak, C. Terashima, K. Nakata, A. Fujishima, U. Paik and Y. S. Kang, *Phys. Chem. Chem. Phys.*, 2014, **16**, 17748–17755.
30 A. Devadoss, P. Sudhagar, S. Das, S. Y. Lee, C. Terashima, K. Nakata, A. Fujishima, W. Choi, Y. S. Kang and U. Paik, *ACS Appl. Mater. Interfaces*, 2014, **6**, 4864–4871.
31 P. A. Morris Hotsenpiller, J. D. Bolt, W. E. Farneth, J. B. Lowekamp and G. S. Rohrer, *J. Phys. Chem. B*, 1998, **102**, 3216–3226.
32 A. Fujishima, X. Zhang and D. A. Tryk, *Surf. Sci. Rep.*, 2008, **63**, 515–582.
33 J. Yu, J. Low, W. Xiao, P. Zhou and M. Jaroniec, *J. Am. Chem. Soc.*, 2014, **136**, 8839–8842.
34 R. Gottesman, S. Tirosh, H.-N. Barad and A. Zaban, *J. Phys. Chem. Lett.*, 2013, **4**, 2822–2828.
35 C. Liu, X. Han, S. Xie, Q. Kuang, X. Wang, M. Jin, Z. Xie and L. Zheng, *Chem. – Asian J.*, 2013, **8**, 282–289.
36 M. Mrowetz, W. Balcerski, A. J. Colussi and M. R. Hoffmann, *J. Phys. Chem. B*, 2004, **108**, 17269–17273.
37 Y. Cong, J. Zhang, F. Chen and M. Anpo, *J. Phys. Chem. C*, 2007, **111**, 6976–6982.
38 C. Burda, Y. Lou, X. Chen, A. C. S. Samia, J. Stout and J. L. Gole, *Nano Lett.*, 2003, **3**, 1049–1051.
39 J. Hensel, G. Wang, Y. Li and J. Z. Zhang, *Nano Lett.*, 2010, **10**, 478–483.
40 A. D. Rakić, A. B. Djurišić, J. M. Elazar and M. L. Majewski, *Appl. Opt.*, 1998, **37**, 5271–5283.
41 P. Sudhagar, K. Asokan, E. Ito and Y. S. Kang, *Nanoscale*, 2012, **4**, 2416–2422.
42 N. C. Saha and H. G. Tompkins, *J. Appl. Phys.*, 1992, **72**, 3072–3079.
43 Y. Nosaka, M. Matsushita, J. Nishino and A. Y. Nosaka, *Sci. Technol. Adv. Mater.*, 2005, **6**, 143.
44 C. Di Valentin, E. Finazzi, G. Pacchioni, A. Selloni, S. Livraghi, M. C. Paganini and E. Giamello, *Chem. Phys.*, 2007, **339**, 44–56.
45 S.-Y. Du and Z.-Y. Li, *Opt. Lett.*, 2010, **35**, 3402–3404.
46 X. Zhang, Y. L. Chen, R.-S. Liu and D. P. Tsai, *Rep. Prog. Phys.*, 2013, **76**, 046401.
47 A. V. Puga, A. Forneli, H. García and A. Corma, *Adv. Funct. Mater.*, 2014, **24**, 240.
48 H. Tada, T. Mitsui, T. Kiyonaga, T. Akita and K. Tanaka, *Nat. Mater.*, 2006, **5**, 782–786.
49 Y. Sun, Z. Sun, S. Gao, H. Cheng, Q. Liu, J. Piao, T. Yao, C. Wu, S. Hu, S. Wei and Y. Xie, *Nat. Commun.*, 2012, **3**, 1057.
50 Y. Wei, L. Ke, J. Kong, H. Liu, Z. Jiao, X. Lu, H. Du and X. W. Sun, *Nanotechnology*, 2012, **23**, 235401.
51 S. Y. Reece, J. A. Hamel, K. Sung, T. D. Jarvi, A. J. Esswein, J. J. H. Pijpers and D. G. Nocera, *Science*, 2011, **334**, 645–648.


 